



HAL
open science

Surface enhanced resonant Raman scattering in hybrid MoSe₂@Au nanostructures

Inès Abid, Weibing Chen, Jiangtan Yuan, Sina Najmaei, Emil Peñafiel,
Renaud Péchou, Nicolas Large, Jun Lou, Adnen Mlayah

► **To cite this version:**

Inès Abid, Weibing Chen, Jiangtan Yuan, Sina Najmaei, Emil Peñafiel, et al.. Surface enhanced resonant Raman scattering in hybrid MoSe₂@Au nanostructures. *Optics Express*, 2018, 26 (22), pp.29411. 10.1364/OE.26.029411 . hal-01921184

HAL Id: hal-01921184

<https://hal.science/hal-01921184>

Submitted on 24 Jun 2019

HAL is a multi-disciplinary open access archive for the deposit and dissemination of scientific research documents, whether they are published or not. The documents may come from teaching and research institutions in France or abroad, or from public or private research centers.

L'archive ouverte pluridisciplinaire **HAL**, est destinée au dépôt et à la diffusion de documents scientifiques de niveau recherche, publiés ou non, émanant des établissements d'enseignement et de recherche français ou étrangers, des laboratoires publics ou privés.



Surface enhanced resonant Raman scattering in hybrid MoSe₂@Au nanostructures

INÈS ABID,¹ WEIBING CHEN,² JIANGTAN YUAN,² SINA NAJMAEI,³ EMIL C. PEÑAFIEL,⁴ RENAUD PÉCHOU,¹ NICOLAS LARGE,^{4,6} JUN LOU,^{2,7} AND ADNEN MLAYAH^{1,5,*}

¹CEMES, Université de Toulouse, CNRS, UPS, Toulouse, France

²Department of Materials Science and NanoEngineering, Rice University, 6100 Main Street, Houston, Texas 77005, USA

³United States Army Research Laboratories, Sensors and Electron Devices Directorate, 2800 Powder Mill Road, Adelphi, Maryland 20783, USA

⁴Department of Physics and Astronomy, The University of Texas at San Antonio, San Antonio, One UTSA Circle, Texas 78249, USA

⁵LAAS, Université de Toulouse, CNRS, UPS, Toulouse, France

⁶nicolas.large@utsa.edu

⁷jlou@rice.edu

*mlyah@cemes.fr

Abstract: We report on the surface enhanced resonant Raman scattering (SERRS) in hybrid MoSe₂@Au plasmonic-excitonic nanostructures, focusing on the situation where the localized surface plasmon resonance of Au nanodisks is finely tuned to the exciton absorption of monolayer MoSe₂. Using a resonant excitation, we investigate the SERRS in MoSe₂@Au and the resonant Raman scattering (RRS) in a MoSe₂@SiO₂ reference. Both optical responses are compared to the non-resonant Raman scattering signal, thus providing an estimate of the relative contributions from the localized surface plasmons and the confined excitons to the Raman scattering enhancement. We determine a SERRS/RRS enhancement factor exceeding one order of magnitude. Furthermore, using numerical simulations, we explore the optical near-field properties of the hybrid MoSe₂@Au nanostructure and investigate the SERRS efficiency dependence on the nanodisk surface morphology and on the excitation wavelength. We demonstrate that a photothermal effect, due to the resonant plasmonic pumping of electron-hole pairs into the MoSe₂ layer, and the surface roughness of the metallic nanostructures are the main limiting factors of the SERRS efficiency.

© 2018 Optical Society of America under the terms of the [OSA Open Access Publishing Agreement](#)

1. Introduction

After the success of graphene-enhanced Raman scattering (GERS) technique [1,2], much effort has been made to explore the potential use of two-dimensional (2D) materials with similar layered structures such as h-BN and transition metal dichalcogenides (TMDs; *e.g.*, MoS₂, WS₂, MoSe₂, WSe₂, and MoTe₂) as SERS substrates [3–7]. In that case, the enhancement of the Raman signal is attributed to the chemical mechanism associated with the charge transfer between the adsorbate and the surface [5].

Recently, there have been several published works on the hybridization of TMDs with plasmonic nanostructures, combining the ideally flat surface of the 2D materials with the electric near-field enhancement induced by localized surface plasmon resonances (LSPR). Uniform and reproducible strong Raman signal was reported for MoS₂ nanosheets decorated with gold nanoparticles [3,5,8–11]. The interaction between the metallic nanostructures and the 2D materials is mediated by the localized surface plasmon (LSP) near-field [12] and dictates the detection sensitivity. A detection limit of 10⁻¹² M was obtained with these hybrid substrates [11], making them very promising for biosensing applications. Previous studies

have reported a strong plasmon-induced surface enhanced Raman scattering (SERS) of TMDs layers [13–16]. The reported studies to date deal with plasmonic nanoparticles randomly deposited on top of the TMD layer [13–18]. In these works, SERS has been utilized to probe the local strain imposed to the TMD layer by the metal nanoparticles [15,18]. Thermal measurements at the monolayer scale are made accessible owing to the SERS, as shown by Zhang *et al.* in the case of MoS₂ and WS₂ monolayers hybridized with Ag nanoparticles [14].

In this work we report on surface-enhanced resonant Raman scattering (SERRS) in hybrid MoSe₂@Au nanostructures. Upon growth, the MoSe₂ layer was transferred onto a gold nanodisk array, thus minimizing strain and stress effects while optimizing the near-field interaction between the TMD layer and the plasmonic excitations. The size and separation of the nanodisks are selected to achieve a fine spectral tuning of the gap plasmons of the nanodisks to the excitons confined in the 2D layer, thus resulting in Fano interference. We investigate the resonant Raman scattering of the hybrid TMD/Au system in this particular regime. Indeed, the Raman scattering is excited either off- or on-resonance with the coupled plasmon-exciton transition. It is systematically compared to the Raman scattering properties of a MoSe₂@SiO₂ layer which provides a mean of estimating the enhancement factor of SERRS with respect to the resonant Raman scattering (RRS). This also allows for addressing the relative contribution of the LSP and the confined excitons to the Raman scattering process. Based on experiments and numerical simulations we unravel the impact of the photothermal effect and of the nanodisk surface roughness on the SERRS enhancement. To the best of our knowledge, this work reports the first observation of SERRS in graphene-like 2D materials.

2. Sample preparation and experimental details

Gold nanodisks were fabricated using the shaped nanosphere lithography [19]. Briefly, a solution containing 250 nm polystyrene nanospheres was spin-coated onto a quartz substrate at 3,000 rpm for 50 s. A closely packed monolayer of spheres was obtained after evaporation of the solvent. Then, an argon/oxygen ion etching process was used to modify the nanosphere size. When increasing the exposure time from 50 to 75 s, the diameter of the nanospheres could be reduced from 190 to 130 nm. Then, 50 nm of Ni was evaporated by e-beam evaporation. The polystyrene nanospheres were mechanically removed using adhesive tape. After cleaning from the polystyrene residue in acetone and ultrasonic bath, a 2 nm-thick Ti adhesion layer followed by a 16 nm-thick Au layer were evaporated. Finally, the nickel was removed by sonication in HNO₃. The average diameter of the so-obtained nanodisks is 140 nm and their edge-to-edge separation is around 50 nm [19].

The MoSe₂ was grown by chemical vapor deposition (CVD) on a silicon substrate capped with 90 nm silica. The substrate was exposed to MoO₃ and pure selenium powder in a high temperature quartz tube furnace. During the growth process the tube was kept under nitrogen gas flow at 750 °C. At this temperature the MoO₃ powder was reduced to MoO_{3-x} by the Se vapor, thus leading to the nucleation and the growth of large crystalline area of multi- and monolayer MoSe₂ [20,21].

To transfer the MoSe₂ layers on the plasmonic substrate, a soft lift-off process was used. The as-grown MoSe₂ was first coated with PMMA and then dipped into a KOH solution for 6 to 12 h, until the silicon substrate was completely etched away. The PMMA/MoSe₂ floating at the surface of the solution was scooped using the gold nanodisks substrate. Finally, the PMMA was removed with acetone and dried under nitrogen flow.

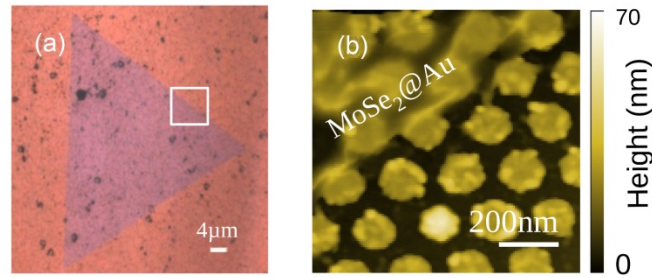


Fig. 1. (a) Bright-field optical image of MoSe₂ monolayer transferred onto Au nanodisks. (b) AFM image recorded from the region marked by the white square in panel (a).

Figure 1(a) displays an optical image of a MoSe₂ monolayer transferred onto Au nanodisks. The monolayer thickness was confirmed by the strong photoluminescence (PL) emission typical of the direct band gap radiative recombinations of the lower energy A excitons [22]. AFM imaging [Fig. 1(b)] and height profiles analysis (not shown), clearly reveal the MoSe₂ layer coating the Au nanodisks and suspended in the gap region between the nanodisks. The AFM data also show height fluctuations due to the surface roughness of the Au nanodisks [Fig. 1(b)] as well as inhomogeneities of the nanodisk diameter and spacing which may strongly influence the optical properties of the system as will be discussed below [23].

Optical transmission measurements under confocal microscope were performed in different regions of the sample where the MoSe₂ layer covers the gold nanodisks as well as the SiO₂ substrate.

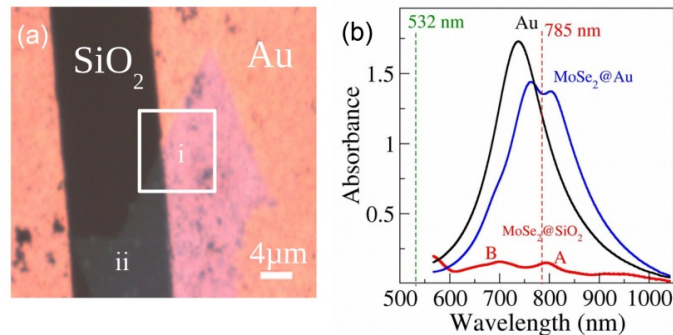


Fig. 2. (a) Bright-field optical image of a MoSe₂ monolayer covering the Au nanodisks (region i) and the SiO₂ substrate (region ii). (b) Optical absorbance spectra in the regions MoSe₂@Au (blue), MoSe₂@SiO₂ (red), and on bare Au nanodisks (black). The vertical dashed lines indicate the non-resonant (532 nm) and resonant (785 nm) laser wavelengths used to excite the Raman scattering.

The optical absorption spectrum of MoSe₂@SiO₂ [Fig. 2(b), red curve] exhibits A and B excitonic peaks at 795 and 700 nm, respectively, in good agreement with previous works [22,24]. Due to the change in the surrounding medium, the optical resonance of MoSe₂@Au [Fig. 2(b), blue curve] is red-shifted with respect to the LSPR of the bare nanodisks [25]. Additionally, a dip is observed at the exciton wavelength. Large and associates have previously shown that interaction between the LSPR of the Au nanodisks and confined excitons is determined by the electric near-field distribution in the gap region between the metal nanoparticles [12]. While in the strong coupling regime, a Rabi splitting occurs [12], the intermediate coupling in our MoSe₂@Au system translates into a Fano interference between the plasmonic and excitonic resonances [25–27] which leads to the formation of the dip in the optical spectrum as shown in Fig. 2(b).

As depicted in Fig. 3(a), the 785 nm laser wavelength is suitable for resonant excitation of both the coupled plasmon-exciton transition of the $\text{MoSe}_2@Au$ system and the confined A-exciton transition of the $\text{MoSe}_2@SiO_2$. This allows for investigating both SERRS and RRS signals, respectively, and hence tracking the relative contribution of the surface plasmons and of the confined excitons to the resonant Raman scattering process.

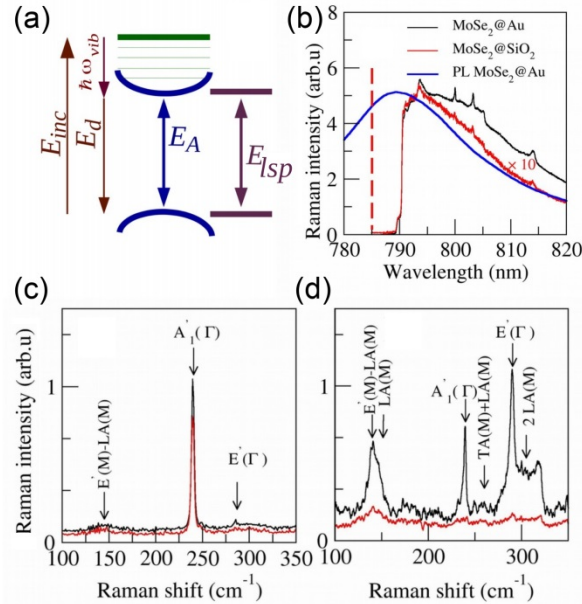


Fig. 3. (a) Energy diagram of the SERRS process mediated by the coupled plasmon-exciton states. E_{LSP} and E_A refer to the LSP and A-exciton energies, respectively. E_{inc} represents the incident energy, E_d is the Raman diffused energy, and $\hbar\omega_{vib}$ stands for the MoSe₂ phonon energy. (b) SERRS (black) and RRS (red) spectra of $\text{MoSe}_2@Au$ and $\text{MoSe}_2@SiO_2$, respectively, excited at 785 nm wavelength (vertical dashed line). The PL spectrum obtained at 532 nm is also shown (blue). The sharp cut-off around 790 nm is due to the spectral edge of the filter used for rejection of the Rayleigh scattering. (c) Off-resonance Raman spectra of $\text{MoSe}_2@Au$ (black) and $\text{MoSe}_2@SiO_2$ (red) excited at 532 nm. (d) SERRS and RRS spectra, shown in panel (b), corrected from the PL background.

Figure 3(b) displays the SERRS and RRS spectra recorded from the $\text{MoSe}_2@Au$ and $\text{MoSe}_2@SiO_2$ regions shown in Fig. 2(a). The Raman features are superimposed upon the excitonic PL background. It is worth mentioning that the laser intensity was kept as low as possible ($2.4 \times 10^4 \text{ W/cm}^2$) to limit the sample heating, thus explaining the weak Raman signals. The observed Raman peaks are assigned to the in-plane (E') and out-of-plane (A'_1) vibration modes of the Mo–Se bonds and also to second-order Raman scattering involving two-phonon emission at the M-point of the Brillouin zone, in agreement with previously reported assignments [Figs. 3(b) and 3(d)] [28,29]. Figure 3(b) shows a clear plasmonic enhancement of the PL emission in $\text{MoSe}_2@Au$, as previously reported for similar hybrid plasmonic-TMD systems [30–34]. To bring up the difference between the SERRS and RRS spectra, we subtracted the PL background. The resulting Raman spectra clearly show an enhancement of the Raman scattering in $\text{MoSe}_2@Au$ as compared to $\text{MoSe}_2@SiO_2$. Moreover, by comparing the Raman spectra recorded off- and in-resonance [Figs. 3(c) and 3(d)], one can see that the enhancement is observed only for resonant excitation of the plasmon-exciton coupled transition (Fig. 2). Indeed, for off-resonance excitation at 532 nm [Fig. 3(c)], the Raman spectra of $\text{MoSe}_2@Au$ and $\text{MoSe}_2@SiO_2$ are very similar. Notice that in that case, due to the large numerical aperture of the microscope objective, which introduces a polarization component perpendicular the Au disks plane, a residual enhancement by the

transverse LSPR of the Au nanodisks cannot be ruled out. This could be responsible for the slightly higher Raman intensity measured for MoSe₂@Au [Fig. 3(c), black spectrum].

3. RRS vs SERRS

In order to investigate more quantitatively the Raman scattering properties of the hybrid MoSe₂@Au nanostructures, we have systematically measured the Raman response inside the region of the sample delimited by the white square in Fig. 2(a). This area is particularly interesting because the MoSe₂ covers the gold nanodisks as well as the SiO₂ substrate, which allows for a direct comparison of the Raman signatures of both MoSe₂@Au and MoSe₂@SiO₂ under exactly the same experimental conditions. Figure 4 shows the spatial distributions of the enhancement factor measured with 532 and 785 nm excitation.

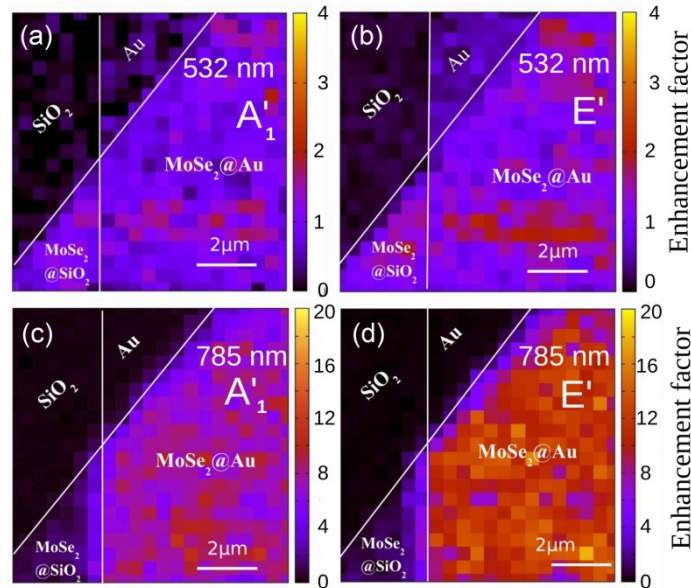


Fig. 4. Enhancement factors of the Raman scattering intensities of the A₁' and E' modes mapped in the squared delimited region shown in Fig. 2, for non-resonant 532 nm (a,b) and resonant 785 nm (c,d) excitations.

The enhancement factor (*EF*) is defined as the local intensity $I_{A'_1, E'}(x, y)$ of either the A₁' or the E' Raman feature, normalized to its average value $\langle I_{A'_1, E'} \rangle_{\text{MoSe}_2@SiO_2}$ measured on the MoSe₂@SiO₂:

$$EF(x, y) = \frac{I_{A'_1, E'}(x, y)}{I_{A'_1, E'}_{\text{MoSe}_2@SiO_2}}. \quad (1)$$

Figures 4(a) and 4(b) show, that there is no significant enhancement of the Raman intensity of neither the A₁' nor the E' mode for off-resonance excitation. Indeed, for an excitation at 532 nm, the Raman features in the MoSe₂@Au and MoSe₂@SiO₂ regions have comparable intensities and the enhancement factor is $EF \sim 1$, thus confirming the absence of any significant contribution of the Au nanodisks LSPR to the Raman scattering process, as already observed in Fig. 3(c).

On the contrary, under resonant excitation at 785 nm [Figs. 4(c) and 4(d)], the Raman scattering in the MoSe₂@Au region is clearly enhanced by more than one order of magnitude as compared to that in the MoSe₂@SiO₂ region, in agreement with the results reported in Fig. 3(d); the SERRS/RRS enhancement factor is around 16 for E' mode and 12 for A₁' mode [Figs. 4(c) and 4(d)]. For conventional plasmon-induced SERS, the SERS/RS enhancement

factor can be as high as seven orders of magnitude [35]. The SERRS/RRS enhancement reported here is much weaker. To fully understand the SERRS response of our system, let us delve deeper into the Raman scattering process mediated by the coupled plasmon-exciton states.

First, it is important to underline that we are comparing two resonant Raman processes: one is plasmon-exciton mediated (*i.e.*, SERRS) and the second is only exciton mediated (*i.e.*, RRS). The latter is already much more efficient than a non-resonant Raman scattering process (at least for the E' mode), thus leading to a smaller SERRS/RRS ratio compared to SERRS/RS.

Second, the Raman laser probe may induce a significant heating of the sample since the optical excitation (785 nm) is doubly resonant with both the LSP and the confined exciton transition. In a previous work, we have demonstrated that a MoS₂ monolayer transferred onto gold nano-antennas experiences a significant photo-induced temperature increase of 74 °C [30]. This photothermal effect was attributed to the energy relaxation of the hot electrons and holes photogenerated in the 2D layer by the plasmonic near-field. In that situation, the LSPR of the Au nano-antenna occurred at higher energy compared to the absorption edge of the MoS₂ layer and was clearly detuned with respect to the A and B exciton transitions. In our MoSe₂@Au system, the LSPR of the Au nanodisks is tuned to the A exciton transition which results in additional enhancement of the absorption and induced photothermal process.

4. Plasmon-exciton induced photothermal effect

In order to investigate more precisely the photothermal effect, we have analyzed the PL emission background [Fig. 3(b)]. As mentioned above, this PL emission arises from the radiative recombination of the A excitons; its intensity, red-shift, and broadening, are distinctive characteristics of sample heating [30]. Therefore, we have extracted these parameters using a Gaussian lineshape fitting to the experimental spectra recorded inside the region shown in Fig. 2(a).

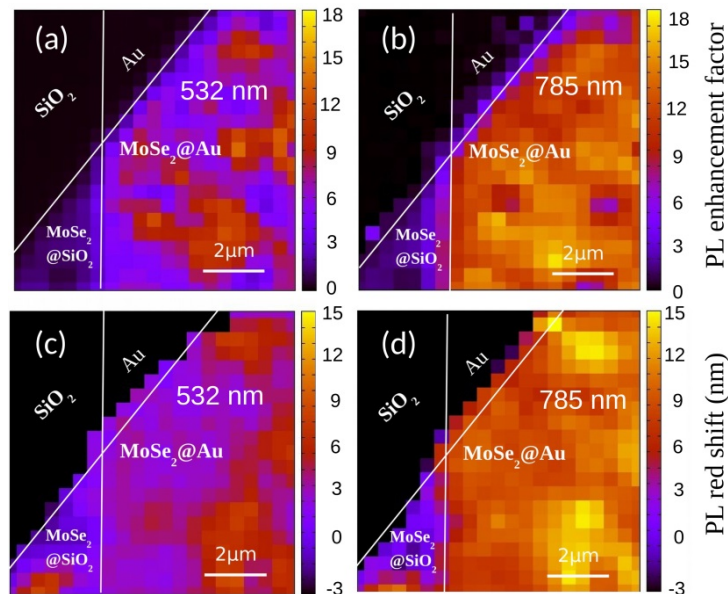


Fig. 5. Enhancement factor (a,b) and wavelength (c,d) of the photoluminescence emission mapped inside the region shown in Fig. 2. The photoluminescence was excited out of resonance (532 nm; a,c) and in resonance (785 nm; b,d) with the coupled plasmon-exciton absorption peak.

As for the Raman scattering, the PL enhancement factor at each point was obtained by normalizing the local PL intensity $I_{\text{PL}}(x,y)$ with respect to its value $\langle I_{\text{PL}} \rangle_{\text{MoSe}_2@SiO_2}$ averaged in the $\text{MoSe}_2@SiO_2$ region:

$$EF_{\text{PL}}(x,y) = \frac{I_{\text{PL}}(x,y)}{\langle I_{\text{PL}} \rangle_{\text{MoSe}_2@SiO_2}}. \quad (2)$$

We define the wavelength shift $\Delta\lambda$ at each point (x,y) as the difference between the local PL emission wavelength $\lambda_{\text{PL}}(x,y)$ and the average emission wavelength $\langle \lambda_{\text{PL}} \rangle_{\text{MoSe}_2@SiO_2}$ measured on the $\text{MoSe}_2@SiO_2$ reference region (Fig. 5):

$$\Delta(x,y) = \lambda_{\text{PL}}(x,y) - \langle \lambda_{\text{PL}} \rangle_{\text{MoSe}_2@SiO_2}. \quad (3)$$

It is important to notice that the PL broadening is not a reliable parameter in our experimental configuration because it cannot be determined with an acceptable accuracy due to the small detuning between the excitation and emission wavelengths.

The PL enhancement factor EF_{PL} and the red-shift were recorded for off- and on-resonance excitation of the plasmonic-excitonic transition. As already discussed in [30], the enhancement of the PL emission in hybrid plasmonic/TMD nanostructures is due to both plasmonic enhanced optical absorption and emission. For an off-resonant excitation (532 nm), $EF_{\text{PL}} \sim 7$ due to the plasmonic enhancement of the local density of optical states (LDOS) receiving the radiative emission [25]. For resonant excitation (785 nm), $EF_{\text{PL}} \sim 14$ in average (with local maxima around 18). In that situation, the resonantly absorbed photons are converted into electron-hole pairs, which lose their kinetic energy by phonon emission and finally recombine radiatively. The resulting heating is confirmed by the 10 nm red-shift of PL signal (with respect to $\text{MoSe}_2@SiO_2$) under resonant excitation of the $\text{MoSe}_2@Au$ layer [Fig. 5(d)]. However, this spectral shift does not exceed 4 nm in the case of non-resonant excitation [532 nm, Fig. 5(c)]. Assuming a PL red-shift of 0.15 nm/°C [30], the temperature increase in $\text{MoSe}_2@Au$ (with respect to $\text{MoSe}_2@SiO_2$) is estimated to be 66 °C for the resonant excitation conditions (785 nm).

Additional evidence for the photothermal effect is provided by the dependence of the PL and Raman scattering on the laser irradiation. Indeed, the PL/Raman spectra of $\text{MoSe}_2@Au$ and $\text{MoSe}_2@SiO_2$ excited at 785 nm with laser intensities of 2.4×10^4 , 2.0×10^5 , and 6.6×10^5 W/cm² are presented in Figs. 6(a) and 6(b). Further increase of the laser intensity results in sample damage.

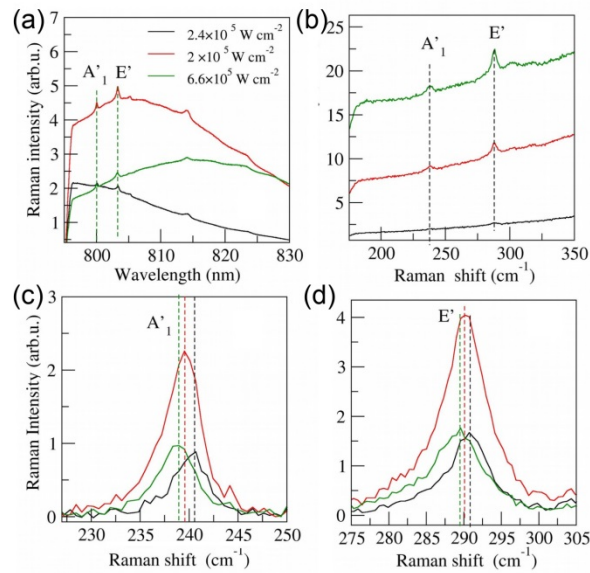


Fig. 6. (a,b) SERRS/PL spectra of $\text{MoSe}_2@Au$ (a) and RRS/PL spectra of $\text{MoSe}_2@SiO_2$ (b), excited at 785 nm with laser intensity $2.4 \times 10^4 \text{ W/cm}^2$ (black), $2.0 \times 10^5 \text{ W/cm}^2$ (red), and $6.6 \times 10^5 \text{ W/cm}^2$ (green). (c,d) Spectra after extraction of the PL signal and zoomed in the spectral region of A'_1 (c) and E' (d) vibration modes. The dashed lines highlight the shift of the Raman peaks.

In the case of $\text{MoSe}_2@SiO_2$ [Fig. 6(b)], the RRS signal of the A'_1 and E' vibration modes increases linearly with increasing laser power, as expected. In the case of $\text{MoSe}_2@Au$ [Fig. 6(a)], the spectra clearly show broadening and red-shift of the PL background with increasing laser excitation intensity. Moreover, the PL intensity exhibits a non-monotonic behavior: a threefold increase, when the laser intensity is increased by a factor of 10, followed by a twofold decrease. The PL intensity drop is confirmed by the red-shift of the Raman peaks of the A'_1 and E' modes [Figs. 6(c) and 6(d)] in good agreement with [36]. On the contrary, no such Raman shift is observed in $\text{MoSe}_2@SiO_2$ when excited at the same laser intensity, which attests the absence of any significant heating in that case (data not shown). It is interesting to comment on the change of the SERRS signal with increasing laser irradiation. As shown in Figs. 6(c) and 6(d) the SERRS intensities of A'_1 and E' modes exhibit a twofold increase with laser intensity increasing from 2.4×10^4 to $2.0 \times 10^5 \text{ W/cm}^2$, and then drop down to their initial levels with further increase of the laser irradiation to $6.6 \times 10^5 \text{ W/cm}^2$. This clearly indicates that heating of the MoSe_2 layer induced by the strong plasmon-exciton absorption of the probe laser light is an important limitation of the SERRS enhancement reported in our $\text{MoSe}_2@Au$ system.

5. Electrodynamic modeling

Since the MoSe_2 layer covers the Au nanodisks, it is significantly embedded in the electromagnetic near-field generated by the surface plasmons. It is therefore interesting to explore the near-field properties of our Fano coupled plasmon-exciton system in connection with the SERRS effect. To do so, we have performed electrodynamic simulations using the discrete dipole approximation (DDA) [37,38]. A model system consisting in a single dimer of gold nanodisks coated with a conformal MoSe_2 monolayer was used in the simulations (Fig. 7) [25,39]. Both the SiO_2 substrate and the Ti adhesion layer were taken into account in the simulations. We chose an inter-dipole spacing of 0.5 nm to ensure full convergence of the calculations. The dimer was optically excited by a plane wave at normal incidence with polarization along the dimer axis. As we have previously shown [39], the lineshape of the

optical spectra [Fig. 2(a)], including the Fano resonance observed at the exciton transition wavelength, are well described using such a model system. We used the refractive index tabulated by Johnson and Christy for Au [40] and the one measured by Liu *et al.* for MoSe₂ [41] using ellipsometry spectroscopy. In this way, the plasmon-exciton interaction is implicitly taken into account at both the excitation and emission steps of the Raman scattering process.

The near-field SERRS gain is calculated using [42]

$$G_{\text{SERRS}} = \left| \frac{\mathbf{E}(\lambda_{\text{inc}})}{\mathbf{E}_{\text{inc}}} \right|^2 \left| \frac{\mathbf{E}(\lambda_{\text{R}})}{\mathbf{E}_{\text{inc}}} \right|^2 \quad (4)$$

where $\mathbf{E}(\lambda_{\text{inc}})$ is the local electric field calculated at the excitation wavelength, $\mathbf{E}(\lambda_{\text{R}})$ is the local electric field at the Raman scattering wavelength, and \mathbf{E}_{inc} is the incident electric field.

In our experiments, the SERRS of MoSe₂@Au is compared to the RRS of MoSe₂@SiO₂. Therefore, we have calculated the electric field excited in a MoSe₂@SiO₂ reference layer and have used its average value to normalize the field in the MoSe₂@Au layer. The gain obtained for the A₁' mode is 1.05 which indicates that the electric field is almost identical to the excitation field in the MoSe₂@SiO₂ layer as expected in the absence of any plasmonic enhancement.

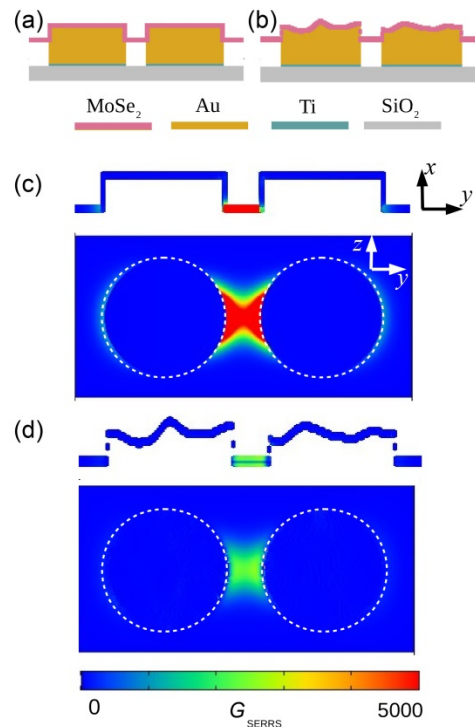


Fig. 7. (a,b) Model system used in the DDA simulations. The disks are 140 nm in diameter and separated by 45 nm gap. The dimer is supported by a SiO₂ (5 nm)/Ti (2 nm) substrate. (c,d) Cross-section and plane views of the SERRS gain within the MoSe₂ layer induced for 785 nm excitation wavelength and at the Raman shift of the A₁' vibration mode for smooth (c) and rough (d) disk surfaces. The excitation field is polarized along the dimer axis.

First, we have calculated the spatial distribution of G_{SERRS} at the Raman shift of the A₁' vibration mode assuming a perfect dimer with smooth nanodisk surfaces [Fig. 7(a)]. As shown in Fig. 7(c), G_{SERRS} reaches a value of 5,000 in the region between the disks. In our

case, the bonding dipole LSP mode interacts with the excitons of the MoSe₂ layer and the Raman excitation (785 nm) is resonant with the plasmon-exciton transition. Figure 8 shows the near-field spectrum of the SERS gain factor $\langle G_{\text{SERRS}} \rangle$ averaged over the entire MoSe₂ layer. The calculated extinction spectrum is also shown for comparison. The maximum of $\langle G_{\text{SERRS}} \rangle$ occurs at 870 nm, red-shifted with respect to the maximum of the far-field extinction spectrum. This red-shift between the near- and far-field spectra has already been reported in the literature [42–44] and was attributed to the surface plasmon damping [44]. It may explain the difference between the measured A₁ and E' SERRS gains (Fig. 4). Indeed, as for SERS, SERRS enhancement depends on the spectral shift between the Raman scattered wavelength λ_{R} and the wavelength at maximum SERS gain [see Eq. (4) and Fig. 8]. The closer λ_{R} is to the maximum of the near-field spectrum, the higher the Raman scattering enhancement. Since the Raman shift of the E' vibration mode is larger than that of the A₁ mode, the corresponding SERRS gain should be slightly higher. As a matter of fact, we found that the average value $\langle G_{\text{SERRS}} \rangle$ at the Raman shift of the E' mode is around 277, whereas that calculated at the Raman shift of the A' mode is around 260.

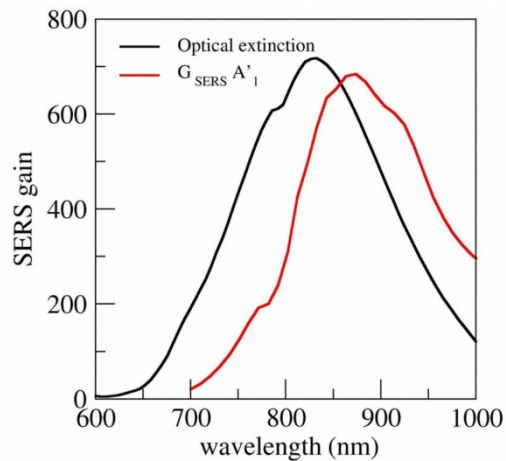


Fig. 8. SERS gain of the modes A₁' as a function of incident wavelength compared with calculated extinction spectrum.

As mentioned above, the calculated values of $\langle G_{\text{SERRS}} \rangle$ are nearly 20 times larger than the experimental values (Fig. 4). In addition to the photothermal effect discussed above, surface roughness of the nanodisks may explain such a difference. In order to investigate this further, we have generated a surface profile of the nanodisks that mimics the actual surface roughness revealed by the AFM measurements [Fig. 1(b)]. The generated surface roughness [Figs. 7(b) and 7(d)] is characterized by an amplitude of 1 nm, a rms of 1 nm, and a correlation length of 20 nm.

Because the LSPR is dictated by the overall shape of the plasmonic nanostructure, the effect of the surface roughness on the extinction spectrum is negligible. However, as it can be seen in Fig. 7(d), the surface roughness strongly affects the near-field intensity: G_{SERRS} drops to 2,000 in the gap region and its average value $\langle G_{\text{SERRS}} \rangle$ over the MoSe₂ layer is around 86 (Fig. 8), which is nearly three times smaller than that calculated for the perfect dimer with smooth disk surfaces. Generally, highly localized electromagnetic hot-spots associated with the surface imperfections yield to an increase of the SERS gain [23,43,45–47]. In our case, the SERRS gain results mainly from the electromagnetic field localized in the gap region between the disks. For perfectly smooth disk surfaces, the overlap between the local field and the MoSe₂ layer in that region is optimal, hence ensuring maximum Raman gain. Surface roughness is responsible for a spatial redistribution of the electromagnetic field that gives rise to the formation of hot-spots outside the gap region. Consequently, the field intensity between

the nanodisks decreases and its overlap with the MoSe₂ is no longer optimal, thus leading to a significant decrease of the Raman gain as compared to the perfectly smooth nanodisk dimer.

6. Summary

Raman scattering of monolayer MoSe₂ transferred on Au nanodisks was investigated in a particular situation where the surface plasmon resonance, localized in the gap between the disks, is tuned to the 2D excitons confined in the MoSe₂ layer.

Using a resonant excitation of the coupled plasmon-exciton states, we were able to measure the SERRS signal of MoSe₂@Au with respect to the RRS of MoSe₂@SiO₂. We found that the SERRS of the A₁' and E' vibration modes of MoSe₂ is enhanced by more than one order of magnitude with respect to the RRS. Although significant, this plasmon-exciton mediated SERRS enhancement is much lower than the one usually reported for SERS. Based on a quantitative analysis of the PL and Raman measurements, we showed that the SERRS gain is limited, by a photothermal effect induced by the resonant excitation of the plasmon-exciton optical transition. The temperature increase, estimated at 66 °C, is responsible for the spectral broadening of the excitonic transition and, consequently, for damping of the optical resonances. On the other hand, using electrodynamic simulations, we have showed that surface roughness of the gold nanodisks strongly impacts the near-field distribution in the gap region between the disks with respect to the smooth surface disks. This, in turn, leads to a significant lowering of the Raman gain, due to the strong dependence of the Raman efficiency on the fourth-power of the local electric field.

It is worth to mention that the absence of a direct band gap in the electronic structure of graphene forbids the SERRS phenomenon. Indeed, the latter requires a direct optical transition spectrally resonant with a localized surface plasmon. That is the reason why SERRS is observable only in 2D TMD materials combined with plasmonic resonators. Of course, different 2D materials from the TMD family (MoS₂, MoSe₂, WS₂, WSe₂, MoTe₂...) exhibit different band gaps and, therefore, the localized surface plasmon resonance has to be tuned accordingly.

Fundamental understanding of the SERS and SERRS in TMDs/metal nanostructures is of prime importance for the engineering of novel devices for sensing applications. Indeed, the combination of Raman scattering mediated by surface plasmons (sustained by metal nanostructures) and charge transfer (in 2D layered materials) is a promising route for highly sensitive molecular sensing. However, the underlying physics still requires both experimental and theoretical investigations in order to reach a high level of control and reliability of sensors based on functional hybrid plasmonic-TMD nanomaterials. The present work sheds light on the Raman scattering properties of hybrid plasmonic-TMD nanostructures. It contributes to uncover the optical properties of TMD-plasmonic systems.

Funding

Programme Investissements d'Avenir (ANR-11-IDEX-0002-02, ANR-10-LABX-0037-NEXT); Welch Foundation (C-1716); Airforce Research Office (FA9550-14-1-0268); Office of Naval Research (N00014-17-1-3024) *via* a subaward from Northwestern University (SP0042269-PROJ0011928); Merle & Helen Converse Scholarship; Ethel W. Bloom Scholarship; Carlos & Malú Alvarez Special Opportunities Fund.

Acknowledgments

We thank Drs. Arash Bohloul and Carolina Avendaño for providing the patterned nanodisk substrates. E.C.P. acknowledges financial support from the Merle & Helen Converse Scholarship, the Ethel W. Bloom Scholarship, and the Carlos & Malú Alvarez Special Opportunities Fund. This work received computational support from UTSA's HPC cluster Shamu, operated by the Office of Information Technology, and HPC center CALMIP at the University of Toulouse.

References

1. W. Xu, X. Ling, J. Xiao, M. S. Dresselhaus, J. Kong, H. Xu, Z. Liu, and J. Zhang, "Surface enhanced Raman spectroscopy on a flat graphene surface," *Proc. Natl. Acad. Sci. U.S.A.* **109**(24), 9281–9286 (2012).
2. N. Zhang, L. Tong, and J. Zhang, "Graphene-based enhanced Raman scattering toward analytical applications," *Chem. Mater.* **28**(18), 6426–6435 (2016).
3. Y. Lee, H. Kim, J. Lee, S. H. Yu, E. Hwang, C. Lee, J.-H. Ahn, and J. H. Cho, "Enhanced Raman scattering of rhodamine 6G films on two-dimensional transition metal dichalcogenides correlated to photoinduced charge transfer," *Chem. Mater.* **28**(1), 180–187 (2016).
4. H. Qiu, Z. Li, S. Gao, P. Chen, C. Zhang, S. Jiang, S. Xu, C. Yang, and H. Li, "Large-area MoS₂ thin layers directly synthesized on pyramid-Si substrate for surface-enhanced Raman scattering," *RSC Advances* **5**(102), 83899–83905 (2015).
5. X. Ling, W. Fang, Y.-H. Lee, P. T. Araujo, X. Zhang, J. F. Rodriguez-Nieva, Y. Lin, J. Zhang, J. Kong, and M. S. Dresselhaus, "Raman enhancement effect on two-dimensional layered materials: Graphene, h-BN and MoS₂," *Nano Lett.* **14**(6), 3033–3040 (2014).
6. P. K. Kannan, D. J. Late, H. Morgan, and C. S. Rout, "Recent developments in 2D layered inorganic nanomaterials for sensing," *Nanoscale* **7**(32), 13293–13312 (2015).
7. C. Muehlethaler, C. R. Consideine, V. Menon, W.-C. Lin, Y.-H. Lee, and J. R. Lombardi, "Ultrahigh Raman enhancement on monolayer MoS₂," *ACS Photonics* **3**(7), 1164–1169 (2016).
8. Z. Li, S. Jiang, Y. Huo, M. Liu, C. Yang, C. Zhang, X. Liu, Y. Sheng, C. Li, and B. Man, "Controlled-layer and large-area MoS₂ films encapsulated Au nanoparticle hybrids for SERS," *Opt. Express* **24**(23), 26097–26108 (2016).
9. S. Su, C. Zhang, L. Yuwen, J. Chao, X. Zuo, X. Liu, C. Song, C. Fan, and L. Wang, "Creating SERS hot spots on MoS₂ nanosheets with in situ grown gold nanoparticles," *ACS Appl. Mater. Interfaces* **6**(21), 18735–18741 (2014).
10. X. Yu, T. Shiraki, S. Yang, B. Ding, and N. Nakashima, "Synthesis of porous gold nanoparticle/MoS₂ nanocomposites based on redox reactions," *RSC Advances* **5**(105), 86558–86563 (2015).
11. S. S. Singha, D. Nandi, and A. Singha, "Tuning the photoluminescence and ultrasensitive trace detection properties of few-layer MoS₂ by decoration with gold nanoparticles," *RSC Advances* **5**(31), 24188–24193 (2015).
12. A. E. Schlather, N. Large, A. S. Urban, P. Nordlander, and N. J. Halas, "Near-field mediated plexcitonic coupling and giant Rabi splitting in individual metallic dimers," *Nano Lett.* **13**(7), 3281–3286 (2013).
13. B. Mukherjee, W. S. Leong, Y. Li, H. Gong, L. Sun, Z. X. Shen, E. Simsek, and J. T. Thong, "Gold on WSe₂ single crystal film as a substrate for surface enhanced Raman scattering (SERS) sensing," *Mater. Res. Express* **2**, 065009 (2015).
14. D. Zhang, Y.-C. Wu, M. Yang, X. Liu, C. Ó. Coileáin, H. Xu, M. Abid, M. Abid, J.-J. Wang, I. V. Shvets, H. Liu, Z. Wang, H. Yin, H. Liu, B. S. Chun, X. Zhang, and H.-C. Wu, "Probing thermal expansion coefficients of monolayers using surface enhanced Raman scattering," *RSC Advances* **6**(101), 99053–99059 (2016).
15. D. Zhang, Y.-C. Wu, M. Yang, X. Liu, C. Ó. Coileáin, M. Abid, M. Abid, J.-J. Wang, I. Shvets, H. Xu, B. S. Chun, H. Liu, and H.-C. Wu, "Surface enhanced Raman scattering of monolayer MX₂ with metallic nanoparticles," *Sci. Rep.* **6**(1), 30320 (2016).
16. J. Y. Kim, J. Kim, and J. Joo, "Surface-enhanced Raman scattering for 2-D WSe₂ hybridized with functionalized gold nanoparticles," *Opt. Express* **24**(24), 27546–27553 (2016).
17. S. Diefenbach, E. Parzinger, J. Kiemle, J. Wierzbowski, S. Funke, B. Miller, R. Csiki, P. Thiesen, A. Cattani-Scholz, U. Wurstbauer, and A. W. Holleitner, "Manifold coupling mechanisms of transition metal dichalcogenides to plasmonic gold nanoparticle arrays," *J. Phys. Chem. C* **122**(17), 9663–9670 (2018).
18. Y. Sun, K. Liu, X. Hong, M. Chen, J. Kim, S. Shi, J. Wu, A. Zettl, and F. Wang, "Probing local strain at MX₂-metal boundaries with surface plasmon-enhanced Raman scattering," *Nano Lett.* **14**(9), 5329–5334 (2014).
19. Z. A. Lewicka, Y. Li, A. Bohloul, W. W. Yu, and V. L. Colvin, "Nanorings and nanocrescents formed via shaped nanosphere lithography: a route toward large areas of infrared metamaterials," *Nanotechnology* **24**(11), 115303 (2013).
20. J. C. Shaw, H. Zhou, Y. Chen, N. O. Weiss, Y. Liu, Y. Huang, and X. Duan, "Chemical vapor deposition growth of monolayer MoSe₂ nanosheets," *Nano Res.* **7**(4), 511–517 (2014).
21. J. Xia, X. Huang, L.-Z. Liu, M. Wang, L. Wang, B. Huang, D.-D. Zhu, J.-J. Li, C.-Z. Gu, and X.-M. Meng, "CVD synthesis of large-area, highly crystalline MoSe₂ atomic layers on diverse substrates and application to photodetectors," *Nanoscale* **6**(15), 8949–8955 (2014).
22. P. Tonndorf, R. Schmidt, P. Böttger, X. Zhang, J. Börner, A. Liebig, M. Albrecht, C. Kloc, O. Gordan, D. R. Zahn, S. Michaelis de Vasconcellos, and R. Bratschitsch, "Photoluminescence emission and Raman response of monolayer MoS₂, MoSe₂, and WSe₂," *Opt. Express* **21**(4), 4908–4916 (2013).
23. Q. Zhang, N. Large, P. Nordlander, and H. Wang, "Porous Au nanoparticles with tunable plasmon resonances and intense field enhancements for single-particle SERS," *J. Phys. Chem. Lett.* **5**(2), 370–374 (2014).
24. Y. Zhang, T.-R. Chang, B. Zhou, Y.-T. Cui, H. Yan, Z. Liu, F. Schmitt, J. Lee, R. Moore, Y. Chen, H. Lin, H.-T. Jeng, S.-K. Mo, Z. Hussain, A. Bansil, and Z.-X. Shen, "Direct observation of the transition from indirect to direct bandgap in atomically thin epitaxial MoSe₂," *Nat. Nanotechnol.* **9**(2), 111–115 (2013).

25. I. Abid, A. Bohloul, S. Najmaei, C. Avendano, H.-L. Liu, R. P echou, A. Mlayah, and J. Lou, "Resonant surface plasmon-exciton interaction in hybrid MoSe₂@Au nanostructures," *Nanoscale* **8**(15), 8151–8159 (2016).
26. A. Manjavacas, F. J. Garcia de Abajo, and P. Nordlander, "Quantum plexcitonics: Strongly interacting plasmons and excitons," *Nano Lett.* **11**(6), 2318–2323 (2011).
27. X. Wu, S. K. Gray, and M. Pelton, "Quantum-dot-induced transparency in a nanoscale plasmonic resonator," *Opt. Express* **18**(23), 23633–23645 (2010).
28. K. Kim, J.-U. Lee, D. Nam, and H. Cheong, "Davydov splitting and excitonic resonance effects in Raman spectra of few-layer MoSe₂," *ACS Nano* **10**(8), 8113–8120 (2016).
29. P. Soubelet, A. E. Bruchhausen, A. Fainstein, K. Nogajewski, and C. Faugeras, "Resonance effects in the Raman scattering of monolayer and few-layer MoSe₂," *Phys. Rev. B* **93**(15), 155407 (2016).
30. S. Najmaei, A. Mlayah, A. Arbouet, C. Girard, J. L eotin, and J. Lou, "Plasmonic pumping of excitonic photoluminescence in hybrid MoS₂-Au nanostructures," *ACS Nano* **8**(12), 12682–12689 (2014).
31. S. Butun, S. Tongay, and K. Aydin, "Enhanced light emission from large-area monolayer MoS₂ using plasmonic nanodisc arrays," *Nano Lett.* **15**(4), 2700–2704 (2015).
32. E. Palacios, S. Park, S. Butun, L. Lauhon, and K. Aydin, "Enhanced radiative emission from monolayer MoS₂ films using a single plasmonic dimer nanoantenna," *Appl. Phys. Lett.* **111**(3), 031101 (2017).
33. B. Lee, J. Park, G. H. Han, H.-S. Ee, C. H. Naylor, W. Liu, A. T. C. Johnson, and R. Agarwal, "Fano resonance and spectrally modified photoluminescence enhancement in monolayer MoS₂ integrated with plasmonic nanoantenna array," *Nano Lett.* **15**(5), 3646–3653 (2015).
34. H. Chen, J. Yang, E. Rusak, J. Straubel, R. Guo, Y. W. Myint, J. Pei, M. Decker, I. Staude, C. Rockstuhl, Y. Lu, Y. S. Kivshar, and D. Neshev, "Manipulation of photoluminescence of two-dimensional MoSe₂ by gold nanoantennas," *Sci. Rep.* **6**(1), 22296 (2016).
35. S. Schl ucker, "Surface-enhanced Raman spectroscopy: Concepts and chemical applications," *Angew. Chem. Int. Ed. Engl.* **53**(19), 4756–4795 (2014).
36. D. J. Late, S. N. Shirodkar, U. V. Waghmare, V. P. Dravid, and C. N. R. Rao, "Thermal expansion, anharmonicity and temperature-dependent Raman spectra of single- and few-layer MoSe₂ and WSe₂," *ChemPhysChem* **15**(8), 1592–1598 (2014).
37. P. J. Flatau and B. T. Draine, "Fast near field calculations in the discrete dipole approximation for regular rectilinear grids," *Opt. Express* **20**(2), 1247–1252 (2012).
38. B. T. Draine and P. J. Flatau, "Discrete-dipole approximation for scattering calculations," *J. Opt. Soc. Am. A* **11**(4), 1491–1499 (1994).
39. I. Abid, W. Chen, J. Yuan, A. Bohloul, S. Najmaei, C. Avendano, R. P echou, A. Mlayah, and J. Lou, "Temperature-dependent plasmon–exciton interactions in hybrid Au/MoSe₂ nanostructures," *ACS Photonics* **4**(7), 1653–1660 (2017).
40. P. B. Johnson and R. W. Christy, "Optical constants of the noble metals," *Phys. Rev. B* **6**(12), 4370–4379 (1972).
41. H.-L. Liu, C.-C. Shen, S.-H. Su, C.-L. Hsu, M.-Y. Li, and L.-J. Li, "Optical properties of monolayer transition metal dichalcogenides probed by spectroscopic ellipsometry," *Appl. Phys. Lett.* **105**(20), 201905 (2014).
42. A.-S. Grimault, A. Vial, and M. Lamy de la Chapelle, "Modeling of regular gold nanostructures arrays for SERS applications using a 3D FDTD method," *Appl. Phys. B* **84**(1–2), 111–115 (2006).
43. D. Kuroski, N. Large, N. Chiang, A.-I. Henry, T. Seideman, G. C. Schatz, and R. P. Van Duyne, "Unraveling the near- and far-field relationship of 2D surface-enhanced Raman spectroscopy substrates using wavelength-scan surface-enhanced Raman excitation spectroscopy," *J. Phys. Chem. C* **121**(27), 14737–14744 (2017).
44. J. Zuloaga and P. Nordlander, "On the energy shift between near-field and far-field peak intensities in localized plasmon systems," *Nano Lett.* **11**(3), 1280–1283 (2011).
45. C. E. Talley, J. B. Jackson, C. Oubre, N. K. Grady, C. W. Hollars, S. M. Lane, T. R. Huser, P. Nordlander, and N. J. Halas, "Surface-enhanced Raman scattering from individual Au nanoparticles and nanoparticle dimer substrates," *Nano Lett.* **5**(8), 1569–1574 (2005).
46. S. J. Lee, Z. Guan, H. Xu, and M. Moskovits, "Surface-enhanced Raman spectroscopy and nanogeometry: The plasmonic origin of SERS," *J. Phys. Chem. C* **111**(49), 17985–17988 (2007).
47. J. Rodr iguez-Fern andez, A. M. Funston, J. P erez-Juste, R. A.  lvarez-Puebla, L. M. Liz-Marz an, and P. Mulvaney, "The effect of surface roughness on the plasmonic response of individual sub-micron gold spheres," *Phys. Chem. Chem. Phys.* **11**(28), 5909–5914 (2009).